



Cite this: *Polym. Chem.*, 2025, **16**, 1713

Stereoregular cyclic poly(3-hydroxybutyrate) enabled by catalyst-controlled tacticity and topology†

Celine R. Parker, ‡ Zhen Zhang, ‡ Ethan C. Quinn, ‡ Liam T. Reilly and Eugene Y.-X. Chen *

Chemocatalytic routes to poly(3-hydroxybutyrate) (P3HB), a natural biodegradable polyester that has long been considered as a more sustainable alternative to non-(bio)degradable polyolefins, can deliver P3HB materials with catalyst-controlled diverse stereomicrostructures for tunable properties. P3HB topology brings in another way of modulating its properties, but selective synthesis of cyclic P3HB is challenging; yet it is harder to simultaneously control both tacticity and topology. Here we introduce an effective strategy to selectively synthesize cyclic isotactic or syndio-rich P3HB by using bulky C_2 -symmetric salen-ligated metal catalysts bearing an initiating ligand that is also a good leaving group, and a relatively long and ionic metal–polymer bond, both facilitating chain end-to-end cyclization. The resulting cyclic P3HB topology has been extensively characterized and differentiated from its linear counterpart, including direct visualization. When compared to its linear counterpart, cyclic P3HB of both stereomicrostructures shows noticeably superior properties, including higher melting and decomposition temperatures, better processability, and higher overall mechanical toughness.

Received 17th November 2024,
Accepted 13th March 2025

DOI: 10.1039/d4py01304b

rsc.li/polymers

Introduction

High-volume commodity plastics, which are typically hard-to-recycle and/or non-(bio)degradable, pose acute environmental concerns due to their growing environmental accumulation and reliance on non-renewable petrochemical feedstocks.^{1–3} In our current global recycling climate, ~22% of plastics escape collection, become pollution, and cause serious concerns towards human, animal, and environmental health and safety.^{4,5} Multifaceted approaches and innovations are required to resolve this issue including, but not limited to, increased participation in the current recycling infrastructure, development of a circular polymer economy, and further consideration of the end-of-life options of new plastics prior to widespread adoption.^{6–11} When contemplating this last facet, the utility of biodegradable plastics becomes apparent.

Poly(3-hydroxyalkanoate)s (PHAs) are a class of bio-sourced and biodegradable polyesters that can breakdown into CO_2 , water, and biomass under managed or unmanaged environments, making them a more sustainable alternative to non-

(bio)degradable plastics.^{12–16} Isotactic poly(3-hydroxybutyrate) (*it*-P3HB) is the most widely studied PHA and is a strong material (ultimate tensile stress, σ_B ~35 MPa) with excellent barriers to gas (water vapor and oxygen) permeation.^{17,18} Biological fermentation routes from biorenewable feedstocks have enabled the commercialization of a few selected PHAs, but large-scale implementation of these PHAs has been limited due to their high production cost and inability to tune PHA properties by varying their stereomicrostructures without changing chemical composition (e.g., by copolymerization).^{19–21} Efforts to reduce the mechanical brittleness of *it*-P3HB by these routes further complicate its synthesis or processing,²² which are better resolved using stereocontrolled chemocatalysis to produce commercially viable P3HB. Examples include the ring-opening polymerization (ROP) of four-membered β -butyrolactone (BBL)^{21,23–25} and stereoselective ROP of the eight-membered *racemic* dimethyl diolide (*rac*-8DL^{Me}), the latter of which has enabled access to stereoperfect *it*-P3HB with quantitative isotacticity (>99% *meso* triads [*mm*]) and melting transition temperature (T_m) being essentially identical to microbial *it*-P3HB.²⁶ In seeking to further enhance PHA material properties, the 8DL platform has been extended to produce PHAs of varying tacticities and side-chain substituents, some of which show polyolefin-like properties.^{27–30}

Seeking to diversify the topology of P3HB available *via* the ROP of 8DL monomers, cyclic P3HB became an attractive syn-

Department of Chemistry, Colorado State University, Fort Collins, CO 80523-1872, USA. E-mail: eugene.chen@colostate.edu

† Electronic supplementary information (ESI) available. See DOI: <https://doi.org/10.1039/d4py01304b>

‡ These authors contributed equally to this work.



thetic target due to its potential for enhanced material properties such as thermal stability and melt-processability. Although early rheological studies had inconclusive results due to linear contaminants in the cyclic polymers of interest,^{31–33} techniques such as high-performance liquid chromatography in the critical condition resolved these issues and enabled the study of the pure cyclic polymers for revealing their distinct material properties.^{34–36} Without chain ends, cyclic polymers exhibit lowered shear viscosities as a result of their reduced entanglement.^{35,37,38} Having no chain ends also reduces their degrees of conformational freedom, resulting in a lower hydrodynamic volumes and radii of gyration relative to linear counterparts.³⁹ Some cyclic polymers have also been shown to have increased degradation temperatures (T_d) over their linear counterparts.^{40–43} Recent synthetic advancements have resulted in production of cyclic polymers able to be topologically characterized without exhaustive refinement.^{43–47} Based on these performance-advantaged properties, cyclic polymers show promise for applications ranging from medicine^{48,49} to electronics^{50–52} and materials science.⁵³

Cyclic polymers were first shown to be a side product formed *via* ring-chain equilibration during polycondensation, the discovery of which laid the foundation of the Jacobsen–Stockmeyer theory and has since sparked a prolific amount of research on the topic of cyclic polymers.^{54–60} Kricheldorf and co-workers first synthesized cyclic polyesters by utilizing cyclic distannoxane initiators through ring-expansion polymerization (REP), producing a series of polyesters from lactone monomers.⁶¹ Utilizing BBL, cyclic, syndio-rich P3HB (*c/sr*-P3HB) with a probability of racemic linkages between two consecutive monomer units (P_r) up to 0.62 was produced. Although this strategy required heating (50–75 °C) for up to 6 days and the polymer retained the hydrolytically unstable distannoxane initiator linkages, making it an unsuitable method for broad implementation. Zwitterionic REP of BBL using an N-heterocyclic carbene, 1,3-dimesitylimidazolin-2-ylidene (SIMes), was then utilized to produce cyclic atactic P3HB (*c/at*-P3HB).⁴⁵ Through omitting the use of a protic initiator, *c/at*-P3HB was also obtained using a zinc oxazinolate catalyst through the proposed back-biting reactions to cleave a labile chain-end.⁶² The resulting cyclic polymer had a nominally higher degradation temperature (temperature at 5% weight loss, $T_{d,5\%}$) than its linear counterpart. The most recent report of *c*-P3HB was synthesized from BBL using an [OSO]-type ligated iron catalyst.⁶³ However, stereocontrolled *c*-P3HB materials with high molar mass and narrow dispersity have been challenging to obtain. Accordingly, this work addresses this challenge *via* the metal-catalyzed ROP of 8DL^{Me} with bulky C_2 -symmetric salen-ligated metal catalysts that can control not only the stereochemistry of the polymerization but also the chain end-to-end cyclization reaction. The catalysts that were discovered from this work to exhibit such catalytic properties are the lanthanum (La)-salen catalysts that carry an initiating ligand that is also a good leaving group, and relatively long and ionic La-OR (polymer) bond, both of which facilitate chain end-to-end cyclization.

Experimental details

Materials

All monomers and catalysts employed in this study were synthesized according to literature procedures.^{26,29,64} Benzyl alcohol (BnOH) and HPLC-grade dichloromethane were stirred for 12 h on activated calcium hydride and distilled before use. All syntheses and manipulations of air- and moisture-sensitive materials were carried out in flamed Schlenk-type glassware on a dual-manifold Schlenk line, on a high-vacuum line, or in an N₂-filled glovebox. Sodium iodide, dithranol, α -cyano-4-hydroxycinnamic acid, trifluoroacetic acid (TFA), sodium trifluoroacetate (NaTFA), 9 kg mol^{−1} polyethylene glycol (PEG), and *trans*-2-[3-(4-*tert*-butylphenyl)-2-propenylidene]malononitrile (DCTB) were obtained from TCI America and used as received. ACS grade tetrahydrofuran, ACS grade chloroform, and ACS grade acetonitrile were obtained from Sigma Aldrich and used as received.

General polymerization procedure

Polymerizations were performed in glass reactors inside an inert N₂ glovebox at ambient temperature (~23 °C). The reactor was first charged with a predetermined amount of monomer and solvent (typically dichloromethane (DCM)), and a mixture of catalyst and/or initiator in solvent was stirred at ambient temperature for 10 minutes in another reactor. The polymerization was initiated by rapid addition of the catalyst solution to the monomer solution. After a desired time, a 0.01 mL of aliquot was taken from the reaction mixture and quenched with a 5% solution of benzoic acid in CDCl₃ for ¹H NMR analysis to obtain the percent monomer conversion data. The polymerization was later quenched by addition of HCl/methanol (5% solution, 20:1 ratio of polymerization solution to quenching solvent). The quenched mixture was then filtered, redissolved in a minimal amount of dichloromethane, and precipitated into an excess amount of cold methanol while stirring. This process was repeated a total of three times and the polymer was then dried in a vacuum oven at 60 °C for 12 h to a constant weight.

Instrumentation

NMR spectroscopy. NMR spectra were recorded on a Varian Inova or Bruker AV-III 400 MHz spectrometer (400 MHz, ¹H; 100 MHz, ¹³C). Chemical shifts for ¹H and ¹³C spectra were referenced to internal solvent resonance 7.26 (chloroform) and are reported as parts per million relative to SiMe₄.

Size-exclusion chromatography. The size-exclusion chromatography (SEC) instrument employed in this study is an Agilent HPLC system equipped with one guard column and two PLgel 5 μ m mixed-C gel permeation columns coupled with a Wyatt DAWN HELEOS II multi (18)-angle light scattering detector and a Wyatt Optilab TrEX dRI detector. Analysis was performed at 40 °C using CHCl₃ as the eluent at a flow rate of 1.0 mL min^{−1}, using Wyatt ASTRA 8.2.0.242 molecular weight characterization software. Samples were run using the “assume 100% mass recovery option” which calculated a dn/dc



internally (~ 0.0254 for *it*-P3HB, ~ 0.0288 for *sr*-P3HB) based on a precisely known polymer concentration of the sample prior to injection, which were $\sim 2.00\text{--}4.00\text{ mg mL}^{-1}$. For the data utilized in the weight-average molar mass (M_w) per elution volume overlays (Fig. 2D), SEC data was obtained while a Wyatt Viscostar III viscometer was equipped to the stack.

Matrix-assisted laser desorption ionization-time-of-flight-mass spectrometry (MALDI-TOF-MS). MALDI-TOF-MS was carried out on a Bruker Microflex LRF mass spectrometer equipped with a Nd:YAG laser at 355 nm and 25 kV accelerating voltage. Polymer solutions were mixed with dithranol matrix solution and co-spotted with NaI salt solution on a ground stainless-steel plate. External calibration was done using the peptide calibration mixture (8 peptides) on a spot adjacent to the sample. The data was processed in the FlexAnalysis software (version 2.4, Bruker Daltonics).

MALDI-TOF-MS was also carried out on a MALDI TOF/TOF UltraflexXtreme high resolution mass spectrometer with a 355 nm modified Nd:YAG laser. Solutions were prepared as 20 : 1 : 1 mixtures of dithranol : analyte : NaTFA and then 1 μL was added to a ground well on a stainless-steel MicroScout plate and allowed to air dry. Similarly a 20 : 1 : 1 mixture of DCTB : PEG : NaTFA solutions was prepared and added to adjacent wells on the plate and allowed to air dry, serving as the external calibration. The raw data was processed in the FlexAnalysis software (version 2.4, Bruker Daltonics).

Atomic force microscopy (AFM). AFM images were obtained under ambient conditions using a Bruker Bioscope Resolve AFM in Peak Force Tapping Scanasyst mode. Silicon cantilevers (SCANASYST-AIR, spring force constant: 0.12 N m^{-1} , frequency: 23 kHz) were used. The samples were prepared under ambient conditions by spin coating (3000 rpm for 30 s, then 4000 rpm for 10 s) freshly cleaved sheets (5 mm^2) of highly ordered pyrolytic graphite (HOPG) with 10 μL of thoroughly dissolved polymer sample solutions (1 mg mL^{-1} and 0.01 mg mL^{-1} in chloroform). Samples were stored under ambient conditions at 23 $^{\circ}\text{C}$ and imaged approximately 2 h after preparation.

Rheology. Shear viscosity measurements were performed on a Discovery Series HR-2 hybrid rheometer (TA Instruments) under nitrogen gas flow (30 psi). Test specimens were loaded between two 8 mm steel electrically heated platen loading discs. Test specimens were trimmed at predetermined temperatures above the T_m of respective polymers. The measurements were performed at gap lengths $\sim 800\text{ }\mu\text{m}$ and an experimental axial force of $\sim 0.2\text{ N}$.

Differential scanning calorimetry (DSC). Differential scanning calorimetry (DSC) was performed on an Auto Q20 TA Instrument on polymer samples (2–4 mg) which were dried at $\sim 60\text{ }^{\circ}\text{C}$ for 12 h prior to analysis. DSC plots show the melting-transition temperature (T_m), glass transition temperature (T_g), crystallization temperature (T_c), and enthalpy of fusion (ΔH_f), obtained from a second heating scan after the thermal history was removed on the first heating scan. The first heating scan was performed at a rate of 10 $^{\circ}\text{C min}^{-1}$, the subsequent cooling scan was performed at a rate of 10 $^{\circ}\text{C min}^{-1}$, followed by a second heating scan that was performed at rate of 10 $^{\circ}\text{C min}^{-1}$.

Thermogravimetric analysis (TGA). Degradation temperatures ($T_{d,5\%}$, defined by the temperature of 5% weight loss) and maximum rate degradation temperatures (T_{\max}) of the polymers were measured by thermal gravimetric analysis (TGA) on a Q50 TGA Analyzer TA Instrument using polymer samples (2–4 mg) which were dried at $\sim 60\text{ }^{\circ}\text{C}$ for 12 h. Samples were heated from ambient temperature to 700 $^{\circ}\text{C}$ at a heating rate of 10 $^{\circ}\text{C min}^{-1}$ under N₂. Values of T_{\max} were obtained from derivative (wt% $^{\circ}\text{C}^{-1}$) vs. temperature ($^{\circ}\text{C}$) plots, while $T_{d,5\%}$ were obtained from wt% vs. temperature ($^{\circ}\text{C}$) plots.

Mechanical testing. Tensile stress/strain testing was performed in an Instron 5966 universal testing system (10 kN load cell) on three dog-bone-shaped test specimens (ASTM D638 standard Type V). The specimens were prepared *via* compression molding using a Carver Auto Series Plus Laboratory Press (Carver, Model 3889.1PL1000, max force 15 ton) with programmable electrically-heated platen (EHP) temperature, and air-/water-controlled cooling. Isolated polymer materials were loaded between non-stick Teflon paper sheets into a stainless-steel mold with inset dimensions 30 \times 73.5 \times 0.41 mm fabricated in-house and compressed between the two EHPs at a clamp force of 5000 psi, at temperature $\sim 5\text{ }^{\circ}\text{C}$ higher than each material's respective T_m for 10 min then the EHPs were turned off and the sample was left under pressure until it reached ambient temperature (slow cooling). Specimens for analysis were generated *via* compression molding and cut using an ASTM D638-5-IMP cutting die (Qualitest) to standard dimensions. From each compression molding procedure using the stainless-steel mold described, three ASTM D638-5 standard dog-bone shaped specimens could be cut. Mechanical performance was averaged for all the specimens measured for each individual species investigated. Thickness (0.30–0.50 mm), width (3.18 mm), and grip length (30.0 mm) of the measured dog-bone specimens were measured for normalization of data by the Bluehill measurement software (Instron). Test specimens were affixed into the screw-tight grip frame. Tensile stress and strain were measured to the point of material break at a grip extension speed of 5.0 mm min^{-1} at ambient conditions. Young's modulus (E , MPa), ultimate strength (σ_B , MPa), yield stress (MPa), and elongation at break (ε_B , %) are obtained from the software analysis.

Results and discussion

Catalyst-controlled synthesis of stereoregular *c*-P3HB

To selectively synthesize stereoregular *c*-P3HB from *rac*-8DL^{Me}, it is of necessity to identify a stereoselective catalyst capable of promoting faster polymerization relative to selective backbiting at the chain end (Fig. 1A). Trityl salen-ligated yttrium silyl amide complex **1** (Fig. 1B), when combined with a stoichiometric amount of BnOH co-initiator, undergoes spontaneous protonolysis to cleave the [Y]–N bond and generate *in situ* the [Y]–OBn active propagating species, and is known to produce *linear*, stereoperfect *it*-P3HB from *rac*-8DL^{Me}.²⁶ The strategy here for the synthesis of *cyclic*, *it*-P3HB (*c*/*it*-P3HB) is to avoid using the BnOH co-initiator, as the bulky silyl amide ligand



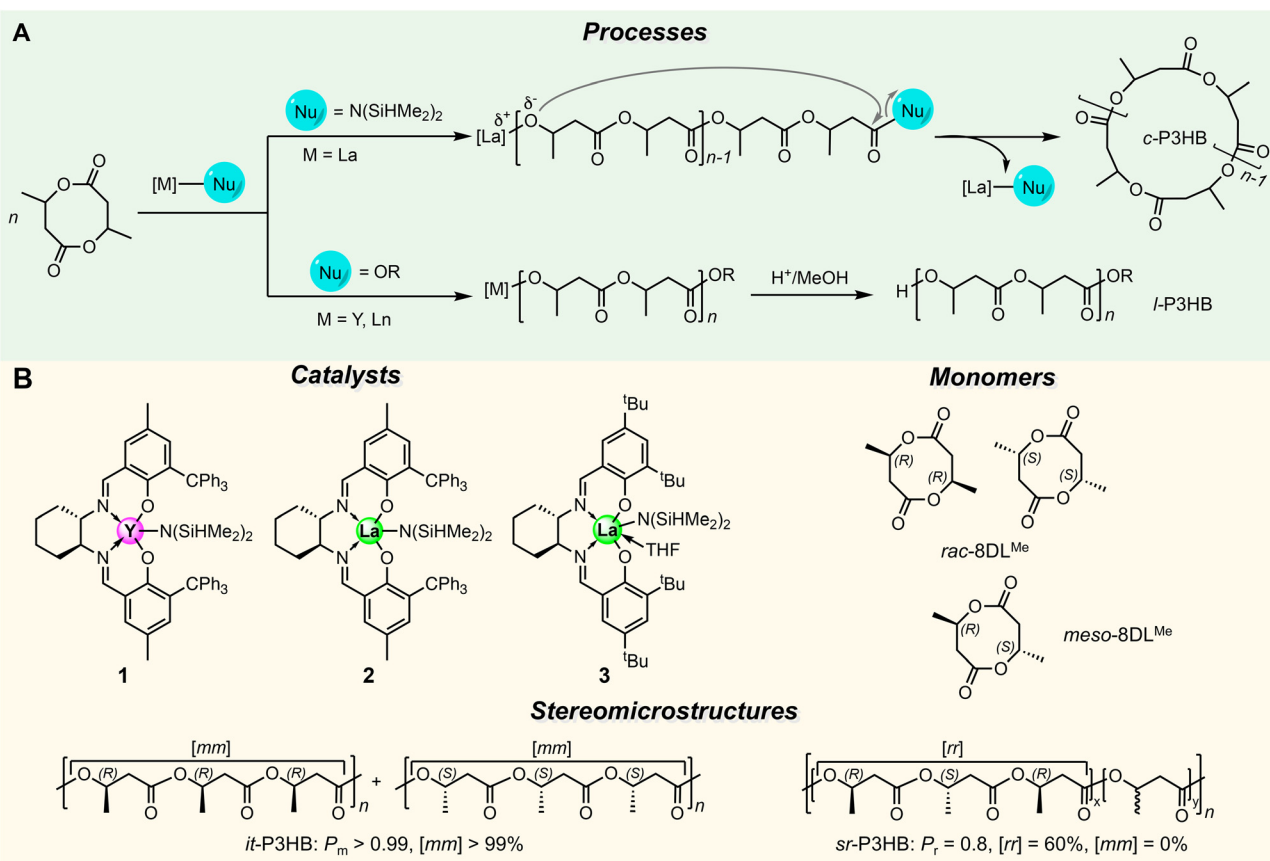


Fig. 1 (A) Sketched synthetic pathways from dimethyl diolide (8DL^{Me}) to linear (*l*) and cyclic (*c*) P3HB. (B) Selected catalysts, monomers, and stereomicrostructures of P3HB discussed herein. All *it*-P3HB discussed is stereo-perfect, with $[mm] > 99\%$.

already present on the precatalyst, $[\text{Y}]\text{-}[\text{N}(\text{SiHMe}_2)_2]$, has been shown to be effective to trigger backbiting by a lanthanum catalyst chain end resulting in end-to-end cyclization.⁴⁰ The challenge is to achieve high selectivity for the cyclic topology and suppress or prevent the formation of mixed linear and cyclic topologies that can result from indiscriminate transesterification along polyester chains.^{65,66} Utilizing this catalyst-controlled cyclization strategy would also enable observing the catalyst's stereoselectivity, thereby achieving the control of both P3HB stereomicrostructures and topologies, which had not been previously reported.

At the outset, *rac*-8DL^{Me} (0.2 M, DCM, $\sim 25^\circ\text{C}$) was polymerized using **1** (5 mol%). After achieving full monomer conversion within 1 min, the reaction was left to cyclize for 7 h, and it was then quenched and analyzed by MALDI-TOF-MS. The resulting MS spectrum (Fig. S1†) of P3HB indicated two series of molecular ion peaks. The lower molar mass series, A, was assigned to *c*-P3HB with no chain ends [$M_{\text{end}} = 0 + 23 \text{ Na}^+ \text{ g mol}^{-1}$] and the higher-molar mass series, B, was assigned to *l*-P3HB with hydroxy/H chain ends [$M_{\text{end}} = 18 + 23 \text{ Na}^+ \text{ g mol}^{-1}$]. Further characterization by ^{13}C NMR (Fig. 2C) revealed that the polymer maintained the desired perfect isotacticity ($[mm] > 99\%$), providing evidence that the stereoselectivity of this catalyst was not impacted by the initiator identity (silyl amide *vs.* alkoxide) (Table 1).

We hypothesized that the effectiveness of the cyclization involving the metal catalyst chain-end and silyl amide (initiating) chain end is affected by the $[\text{M}]\text{-OR}$ bond length and ionic character. Thus, increasing this bond length and ionic character by switching from a group 3 metal (Y) to a lanthanide metal (Ln) possessing a larger ionic radius would allow for more facile backbiting/cyclization reactions leading to the more selective formation of *c*-P3HB. Lanthanum (La) fits these criteria as it has the largest ionic radius of the Ln series^{66,67} and La-based catalysts have previously been shown to be highly active towards the ROP of *rac*- and *meso*-8DL^{Me} producing stereoperfect *it*-P3HB ($M_n = 190 \text{ kg mol}^{-1}$, $D = 1.03$, $P_m > 0.99$) and syndiotactic (*st*-) P3HB ($M_n = 16.9 \text{ kg mol}^{-1}$, $D = 1.09$, $P_r = 0.92$).²⁹ Additionally, $\text{La}([\text{NSiMe}_3]_3)$ has previously been utilized to produce cyclic poly(γ -butyrolactone) and cyclic 3,4-*trans*-cyclohexyl-fused poly(γ -butyrolactone) under neat conditions due to the favorable leaving group ability of the silyl amine chain end that facilitates backbiting from the ionic La-OR (polymer) chain end, inducing cyclization.^{40,68}

Based on the above reasoning, we subsequently employed La-based catalyst **2** (Fig. 1B) for the same ROP ($[\text{rac-8DL}^{\text{Me}}] = 0.2 \text{ M}$, 5 mol% **2**, DCM, $\sim 25^\circ\text{C}$). Gratifyingly, MALDI-TOF-MS analysis of the polymer sample showed the presence of only a single series of molecular ion peaks attributed to *c*-P3HB with



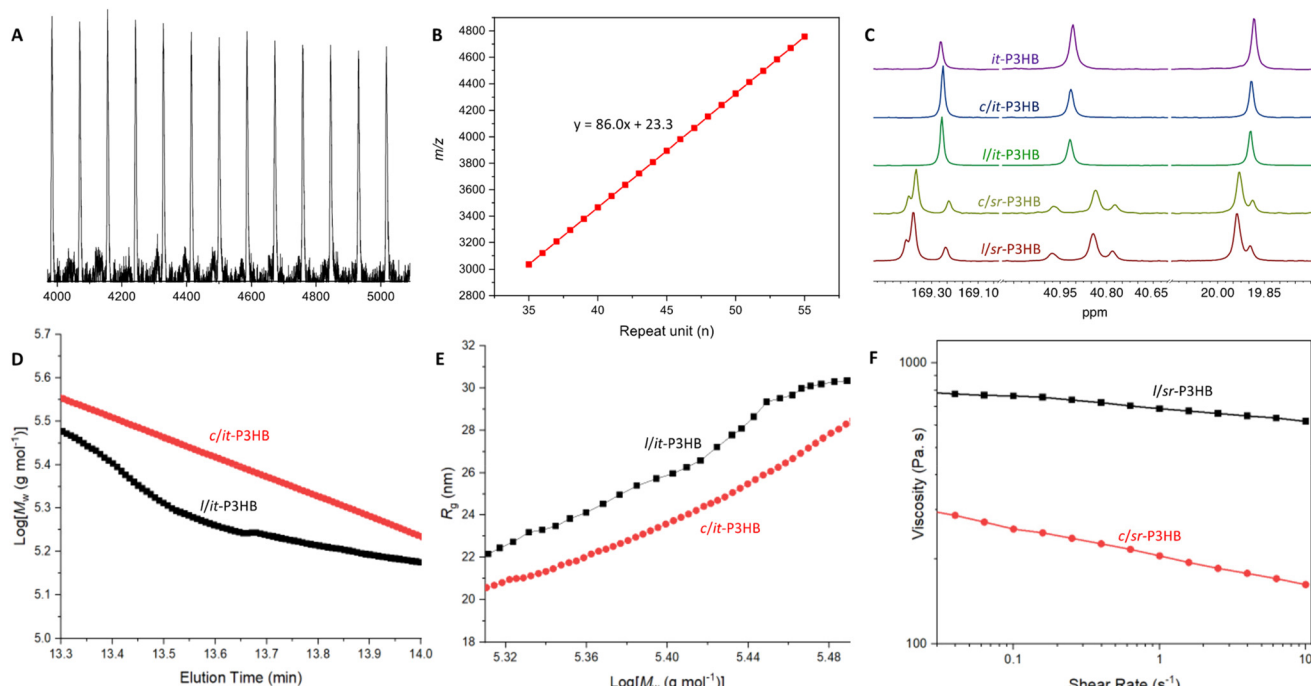


Fig. 2 (A) MALDI-TOF-MS spectrum of *c/it*-P3HB produced using **2**. (B) Plot of the mass-to-charge ratio (m/z) vs. the theoretical number of repeat units for *c/it*-P3HB produced using **2**. (C) ^{13}C NMR overlay of P3HB produced in this work: *it*-P3HB (top, purple) produced using **1**, *c/it*-P3HB (2nd from top, blue) produced using **2**, *I/it*-P3HB (center, green) produced using **2** and BnOH, *c/sr*-P3HB (2nd from bottom, yellow) produced using **3**, *I/sr*-P3HB (bottom, red) produced using **3** and BnOH. (D) Log of weight-average molar mass (M_w , g mol⁻¹) per elution time (as a function of their hydrodynamic radius) of *c/it*-P3HB (red, 164 kg mol⁻¹, D = 1.21) and *I/it*-P3HB (black, 141 kg mol⁻¹, D = 1.07). (E) Radius of gyration (R_g) per log[M_w] of *c/it*- and *I/it*-P3HB. (F) Shear sweeps of *I/sr*-P3HB (black, 152 kg mol⁻¹, D = 1.17) and *c/sr*-P3HB (red, 143 kg mol⁻¹, D = 1.22).

Table 1 Synthesized isotactic and syndio-rich P3HBs with cyclic and linear topologies^a

| P3HB | [M] | Catalyst | M_n ^b (kg mol ⁻¹) | D ^b | P_r ^c | P_m ^c | [mm] ^c (%) | [rr] ^c (%) | [mr] + [rm] ^c (%) |
|---|--------------------------------|----------|--|------------------|--------------------|--------------------|-----------------------|-----------------------|------------------------------|
| <i>c</i> + <i>l/it</i> -P3HB ^d | <i>rac</i> -8DL ^{Me} | 1 | n.d. | n.d. | 0 | >0.99 | >99 | 0 | 0 |
| <i>c/it</i> -P3HB ^e | <i>rac</i> -8DL ^{Me} | 2 | 93.3 | 1.28 | 0 | >0.99 | >99 | 0 | 0 |
| <i>l/it</i> -P3HB ^f | <i>rac</i> -8DL ^{Me} | 2 | 141 | 1.07 | 0 | >0.99 | >99 | 0 | 0 |
| <i>c/sr</i> -P3HB ^g | <i>meso</i> -8DL ^{Me} | 3 | 143 | 1.22 | 0.80 | 0.20 | 0 | 60 | 40 |
| <i>l/sr</i> -P3HB ^h | <i>meso</i> -8DL ^{Me} | 3 | 152 | 1.17 | 0.80 | 0.20 | 0 | 60 | 40 |

^a Reaction conditions unless otherwise stated: no alcohol co-initiator, $[M] = 0.2$ M, dichloromethane (DCM), 7 h, 25 °C. Other details can be found in Table 2. ^b Absolute weight-average molar mass (M_w), number-average molar mass (M_n), and dispersity ($D = M_w/M_n$) determined by size exclusion chromatography (SEC) coupled with a Wyatt DAWN HELEOS II multi (18) angle light scattering detector and a Wyatt Optilab TrEX dRI detector and performed at 40 °C in chloroform. ^c Calculated from semiquantitative ^{13}C NMR (CDCl_3 , 25 °C). ^d Determined as a mixture of cyclic and linear topologies by MALDI-TOF-MS. Molar mass of the oligomers synthesized for MS analysis were not determined (n.d.) by SEC. ^e $[M] = 0.5$ M, 12 h. ^f BnOH as initiator, $[M] = 0.01$ M, 0.5 h. ^g $[M] = 0.1$ M, 12 h. ^h BnOH as initiator, $[M] = 1.0$ M, 7 h.

Table 2 Conversion and molar mass of selected P3HB materials^a

| Sample | Polymer | Catalyst | Concentration (mol L ⁻¹) | [M]/[Cat] equiv. | Time (h) | Conv. (%), ^1H NMR | M_n (kg mol ⁻¹ , SEC) | D |
|--------|--------------------------------|----------|--------------------------------------|------------------|----------|-----------------------------|------------------------------------|------|
| 2 | <i>c/it</i> -P3HB | 2 | 0.5 | 200/1 | 12 | >99 | 93.3 | 1.28 |
| 3 | <i>l/it</i> -P3HB ^b | 2 | 0.01 | 600/1 | 0.5 | >99 | 141 | 1.07 |
| 4 | <i>c/sr</i> -P3HB | 3 | 0.1 | 150/1 | 12 | >99 | 143 | 1.22 |
| 5 | <i>l/sr</i> -P3HB ^b | 3 | 1 | 1000/1 | 7 | 59 | 152 | 1.17 |
| 6 | <i>c/it</i> -P3HB | 2 | 0.005 | 200/1 | 12 | >99 | 164 | 1.21 |
| 7 | <i>l/sr</i> -P3HB ^c | 3 | 1 | 500/1 | 36 | >99 | 283 | 1.26 |
| 8 | <i>c/sr</i> -P3HB | 3 | 1 | 150/1 | 20 | >99 | 162 | 1.28 |

^a Reaction conditions: dichloromethane (DCM), ~25 °C, inert (N_2) atmosphere. ^b Benzyl alcohol (BnOH) used as an initiator (1 eq.). ^c Benzyl alcohol (BnOH) used as an initiator (0.5 eq.).



no chain ends [$M_{\text{end}} = 0 + 23 \text{ Na}^+ \text{ g mol}^{-1}$] (Fig. 2A and B). This result supported the above hypothesis that the longer [M]-OR bond length and higher ionic character facilitates chain end-to-end cyclization, thus leading to selective *c*-P3HB formation, although other alternative cyclization pathways could not be ruled out without further detailed studies to probe all possible cyclization mechanisms. Higher molar mass *c/it*-P3HB can be obtained by simply adjusting the monomer-to-catalyst/initiator ratio. For example, employing the ratio of *rac*-8DL^{Me}:2 = 400:1, the ROP accordingly yielded *c/it*-P3HB with higher molar mass ($M_n = 93.3 \text{ kg mol}^{-1}$, $D = 1.28$).

After accomplishing the synthetic target of *c/it*-P3HB, we tested the hypothesis that this method could be generalized to *c*-P3HB materials with other stereomicrostructures, thanks to the catalyst-site-controlled stereoselectivity. Thus, salen-ligated La catalyst 3 (Fig. 1B) with *tert*-butyl substituents in the *ortho* and *para* positions was selected to polymerize *meso*-8DL^{Me} to *c/*- and *l/sr*-P3HB materials, using 3 alone and 3 + BnOH, respectively, otherwise employing the same conditions. The cyclic topology of *c/sr*-P3HB was again observed by MALDI-TOF-MS (Fig. S2†), confirming the generalizability of the cyclic polymer synthesis strategy. Next, higher-molar mass *sr*-P3HB samples were prepared for further materials testing: *l/sr*-P3HB ($M_n = 152 \text{ kg mol}^{-1}$, $D = 1.17$) and *c/sr*-P3HB ($M_n = 143 \text{ kg mol}^{-1}$, $D = 1.22$). Their tacticities were measured by ¹³C NMR, showing [*mm*] = 0%, [*mr + rm*] = 40%, [*rr*] = 60% and $P_r = 0.80$ for both the cyclic and linear polymers (Fig. 2C), again validating that the identity of the initiating species did not impact the stereoselectivity of this catalyst-site-controlled ROP stereoselectivity.

Characterization of synthesized P3HB topologies

MALDI-TOF-MS is an effective and rapid method to screen the topology of P3HB produced by catalysts 2 and 3, but this method is limited to the low molar-mass range, up to ~ 5000 *m/z* for the P3HB analyzed under the current conditions (Fig. 2A). Upon obtaining higher molar mass samples for cyclic and linear *it*- and *sr*-P3HBs, further characterization was performed to differentiate between the linear and cyclic topologies. First, size-exclusion chromatography (SEC) experiments comparing their weight-average molar mass (M_w) per elution volume showed that *c/it*-P3HB (164 kg mol^{-1} , $D = 1.21$) had higher M_w than *l/it*-P3HB at identical elution times (141 kg mol^{-1} , $D = 1.07$) (Fig. 2D), which aligns with previously observed trends when comparing cyclic and linear polymers.^{33,46,47} This observed trend is due to the fact that cyclic polymers have fewer degrees of conformational freedom compared to their linear counterparts and thus have reduced hydrodynamic volume.³⁹ Next, the radii of gyration (R_g) of *c/it*- and *l/it*-P3HB were measured through multi-angle light scattering and then compared (Fig. 2E). As expected, the R_g values of *c/it*-P3HB were shown to be lower than their linear counterparts.

In an attempt to directly visualize the cyclic topology of *c/it*-P3HB compared with *l/it*-P3HB, atomic force microscopy (AFM) was employed to differentiate these two topologies.

Thin slices of highly ordered pyrolytic graphite (HOPG) were spin coated with dilute solutions of dissolved P3HB and the resulting substrate depositions were subsequently imaged by AFM. Consistently, images of the *c/it*-P3HB sample (170 kg mol^{-1} , $D = 1.26$) comprised of large distinct circular aggregates (Fig. S3†). In sharp contrast, images of *l/it*-P3HB (141 kg mol^{-1} , $D = 1.07$) possessed a strikingly different structural pattern (Fig. S3†). Despite unsuccessfully obtaining images at the single chain level to provide direct topological characterization, the linear and cyclic samples consistently produced contrasting images which allowed for qualitative differentiation between cyclic and linear samples of P3HB with high molar masses. The origin and nature of the apparent differences in substrate deposition/aggregation behavior were not investigated in detail but remain topics of interest.

Thermal, rheological, and mechanical properties of *c*-P3HB

After validating the topology of the respective stereoregular P3HB samples, we subsequently performed comparative studies of their material properties to uncover their performance differences. Initial characterizations by ¹³C NMR revealed that *c/it*-P3HB produced by catalyst 2 also had perfect isotacticity ($P_m > 0.99$, [*mm*] > 99%, Fig. 2C). Consequently, through thermal analysis this *c/it*-P3HB ($M_n = 93.3 \text{ kg mol}^{-1}$, $D = 1.28$) was shown to be a semi-crystalline polymer with a T_m of $174 \text{ }^\circ\text{C}$ and an enthalpy of fusion $\Delta H_f = 106 \text{ J g}^{-1}$ (Fig. 3A, Table 3). This T_m is $4 \text{ }^\circ\text{C}$ higher than its linear analogue ($M_n = 141 \text{ kg mol}^{-1}$, $D = 1.07$) with a $T_m = 170 \text{ }^\circ\text{C}$ ($\Delta H_f = 124 \text{ J g}^{-1}$), which may indicate tighter packing in the crystal lattice of the cyclic polymer than its linear counterpart. Likewise, the crystallization temperature (T_c) of $107 \text{ }^\circ\text{C}$ of *c/it*-P3HB was found to be considerably higher than that ($87.8 \text{ }^\circ\text{C}$) of *l/it*-P3HB (Fig. 3B). The $T_{d,5\%}$ of *c/it*-P3HB was measured to be $245 \text{ }^\circ\text{C}$ which was $10 \text{ }^\circ\text{C}$ higher than *l/it*-P3HB with a $T_{d,5\%}$ of $235 \text{ }^\circ\text{C}$ (Fig. 3C), which can be attributed to the enhanced stability of *c/it*-P3HB conferred by the lack of chain ends. Following the same trend, *c/sr*-P3HB ($M_n = 143 \text{ kg mol}^{-1}$, $D = 1.22$) exhibited a higher T_m of $132 \text{ }^\circ\text{C}$ ($\Delta H_f = 43.0 \text{ J g}^{-1}$) compared to its linear counterpart ($M_n = 152 \text{ kg mol}^{-1}$, $D = 1.17$) with a T_m of $129 \text{ }^\circ\text{C}$ ($\Delta H_f = 35.2 \text{ J g}^{-1}$). Similar to *c/it*-P3HB, *c/sr*-P3HB also exhibited a higher $T_{d,5\%}$ of $252 \text{ }^\circ\text{C}$ than *l/sr*-P3HB which had a $T_{d,5\%}$ of $245 \text{ }^\circ\text{C}$. A combination of increased T_m values due to better packing and enhanced $T_{d,5\%}$ values due to the lack of chain ends demonstrate superior thermal properties of *c*-P3HB to its counterpart *l*-P3HB in both *it* and *sr*-stereomicrostructures.

Based on the enhanced thermal properties associated with *c*-P3HB, further assessment of its melt-processability was conducted by observing its shear viscosity through rheology. It was commonly observed that a cyclic polymer exhibits a lower viscosity than its linear counterpart due to reduced chain entanglement.^{33,35-38,69} Shear sweeps were conducted on *c/sr*-P3HB ($M_n = 143 \text{ kg mol}^{-1}$, $D = 1.22$) and *l/sr*-P3HB ($M_n = 152 \text{ kg mol}^{-1}$, $D = 1.17$). Consistently, the viscosity of *c/sr*-P3HB was found to be considerably lower than its linear counterpart at the same shear rates (Fig. 2F). Reduced viscosity can



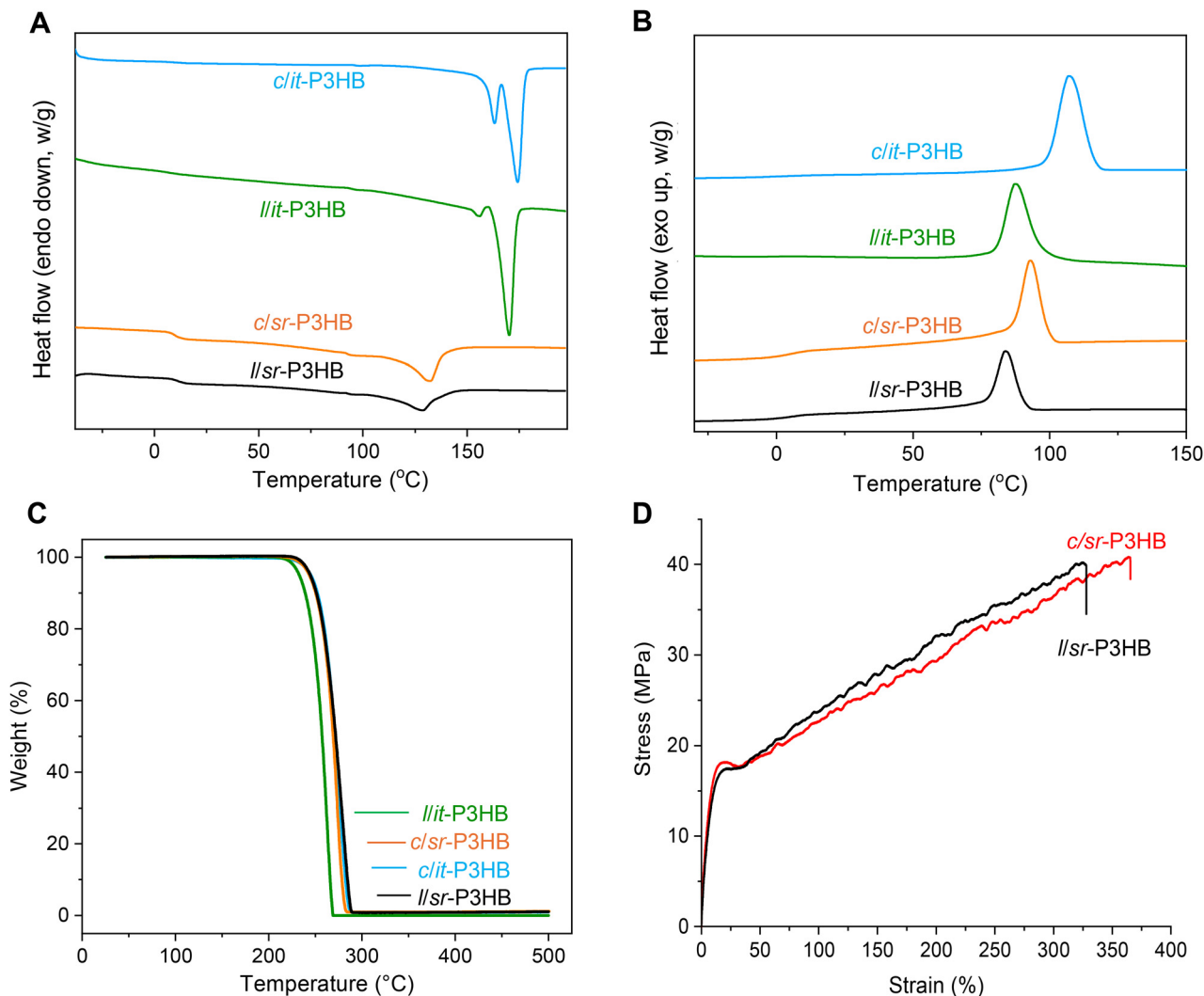


Fig. 3 (A) Overlay of DSC trace, 2nd heating scan ($10\text{ }^{\circ}\text{C min}^{-1}$). (B) Overlay of DSC trace cooling scan ($10\text{ }^{\circ}\text{C min}^{-1}$). (C) Representative stress–strain curves of *l/sr*-P3HB (black, 283 kg mol^{-1} , $D = 1.26$) and *c/sr*-P3HB (red, 163 kg mol^{-1} , $D = 1.28$). Strain rate = 5 mm min^{-1} . (D) Decomposition temperature overlay of P3HB produced in this work.

Table 3 Thermal properties of linear and cyclic P3HB

| P3HB | T_m^a ($^{\circ}\text{C}$) | ΔH_f^a (J g^{-1}) | T_c^a ($^{\circ}\text{C}$) | ΔH_c^a (J g^{-1}) | $T_{d,5\%}^b$ ($^{\circ}\text{C}$) | T_{\max}^b ($^{\circ}\text{C}$) | X_c^c (%) |
|-------------------|-----------------------------------|---|-----------------------------------|---|---|--|----------------|
| <i>c/it</i> -P3HB | 174 | 106 | 107 | 93.6 | 245 | 276 | 73 |
| <i>l/it</i> -P3HB | 170 | 124 | 87.8 | 74.1 | 235 | 259 | 84 |
| <i>c/sr</i> -P3HB | 132 | 43.0 | 92.9 | 56.4 | 252 | 285 | 29 |
| <i>l/sr</i> -P3HB | 129 | 35.2 | 83.7 | 50.0 | 245 | 279 | 24 |

^a Values obtained using differential scanning calorimetry (DSC) at a heating and cooling rate of $10\text{ }^{\circ}\text{C min}^{-1}$. ^b Values obtained using thermogravimetric analysis (TGA) at a heating rate of $10\text{ }^{\circ}\text{C min}^{-1}$.

^c Degree of crystallinity. Calculated according to ESI Note 1.†

enhance processability, therefore *c*-P3HB shows this additional property advantage.

Lastly, mechanical performance was tested by uniaxial tensile testing and compared between *l/sr*-P3HB (283 kg mol^{-1} ,

$D = 1.26$) and *c/sr*-P3HB (163 kg mol^{-1} , $D = 1.28$). Shown to be a tough, ductile thermoplastic, the *l/sr*-P3HB exhibited a Young's modulus (E) = $230 \pm 22\text{ MPa}$, tensile strength (σ) = $38.1 \pm 2.2\text{ MPa}$, and elongation at break (ε_B) = $299 \pm 27\%$. Similarly, the *c/sr*-P3HB was also shown to be a tough, ductile thermoplastic, with noticeably enhanced tensile values (even with a more than 100 kg mol^{-1} lower molar mass): $E = 298 \pm 65\text{ MPa}$, $\sigma = 40 \pm 0.8\text{ MPa}$, and $\varepsilon_B = 375 \pm 11\%$ (Fig. 3D). Overall, the above results showed enhanced thermal, mechanical, and rheological properties of *c*-P3HB over its linear counterpart.

Conclusions

This study has revealed that, in the chemocatalytic synthesis of stereoregular P3HB by the metal-catalyzed ROP of eight-mem-

bered diolide monomers, *rac*-8DL^{Me} and *meso*-8DL^{Me}, the catalyst site can impart control over not only the stereoregularity (e.g., stereoperfect *it*-P3HB and *sr*-P3HB) but also the topology of the resulting P3HB materials. In particular, while the use of the typical [Y]-[N(SiHMe₂)₂] + ROH initiating system leads to formation of *l*-P3HB, removal of the ROH co-initiator triggers generation of a significant portion of *c*-P3HB in the product mixture, due to backbiting cyclization and the silyl-amide being a better leaving group than the typical alkoxide group. More interestingly, simply switching the salen-ligated catalyst's metal center from [Y] to [La], the latter of which exhibits a longer [M]-OR (polymer) length and ionic character, renders selective formation of *c*-P3HB, attributed to enhanced chain end-to-end cyclization upon completion of polymerization.

The linear and cyclic P3HB topologies were characterized and compared extensively, through a suite of analytical techniques, including NMR, MALDI-TOF-MS, SEC, DSC, TGA, rheological and tensile tests, as well as direct visualization by AFM imaging. Most notably, for both types of P3HB stereomicrostructures, *it*-P3HB and *sr*-P3HB, when compared to its linear counterpart, cyclic P3HB demonstrates noticeably superior properties, including higher thermal transitions (T_m and T_c) and decomposition temperature (T_d); better processability (lower shear viscosity); and somewhat but noticeable higher Young's modulus, ultimate tensile strength, fracture stain, and thus overall toughness. While further investigation into the underlying cyclization mechanism is warranted, these results highlight the important role of the [M]-X (X = initiating nucleophile, leaving group, or polymer chain) bond properties (length, ionic character, metal size) in controlling the selectivity of the resulting polymer topology and should stimulate further research on selective synthesis of cyclic polymers with specific property enhancements.

Author contributions

C. R. P., Z. Z., & E. C. Q.: investigation, data curation, writing – original draft, writing – review & editing, visualization, validation, and methodology. L. T. R.: imaging, visualization, writing – review & editing. E. Y.-X. C.: resources, writing – review & editing, supervision, project administration, and funding acquisition.

Data availability

The data supporting this article have been included as part of the ESI.†

Conflicts of interest

There are no conflicts to declare.

Acknowledgements

The work was supported by the U.S. Department of Energy, Office of Energy Efficiency and Renewable Energy, Advanced Materials and Manufacturing Technologies Office (AMMTO), and Bioenergy Technologies Office (BETO), performed as part of the BOTTLE Consortium, which includes the members from Colorado State University, and funded under contract no. DE-AC36-08GO28308 with the National Renewable Energy Laboratory, operated by the Alliance for Sustainable Energy. The authors also thank the Analytical Resources Core (RRID: SCR_021758) and Dr Alyssa Winter May at Colorado State University for instrument access, training, and assistance with sample analysis using the Bruker Ultraflex, which was obtained using NSF grant no. 2117934.

References

- 1 S. B. Borrelle, J. Ringma, K. L. Law, C. C. Monnahan, L. Lebreton, A. McGivern, E. Murphy, J. Jambeck, G. H. Leonard, M. A. Hilleary, M. Eriksen, H. P. Possingham, H. De Frond, L. R. Gerber, B. Polidoro, A. Tahir, M. Bernard, N. Mallos, M. Barnes and C. M. Rochman, *Science*, 2020, **369**, 1515–1518.
- 2 A. Chamas, H. Moon, J. Zheng, Y. Qiu, T. Tabassum, J. H. Jang, M. Abu-Omar, S. L. Scott and S. Suh, *ACS Sustainable Chem. Eng.*, 2020, **8**, 3494–3511.
- 3 R. Geyer, J. R. Jambeck and K. L. Law, *Sci. Adv.*, 2017, **3**, e1700782.
- 4 P. G. C. Nayanathara Thathsarani Pilapitiya and A. S. Ratnayake, *Cleaner Mater.*, 2024, **11**, 100220.
- 5 OECD, *Global Plastics Outlook*, 2022.
- 6 R. W. Clarke, G. Rosetto, T. Uekert, J. B. Curley, H. Moon, B. C. Knott, J. E. McGeehan and K. M. Knauer, *Mater. Adv.*, 2024, **5**, 6690–6701.
- 7 G. W. Coates and Y. D. Y. L. Getzler, *Nat. Rev. Mater.*, 2020, **5**, 501–516.
- 8 L. D. Ellis, N. A. Rorrer, K. P. Sullivan, M. Otto, J. E. McGeehan, Y. Román-Leshkov, N. Wierckx and G. T. Beckham, *Nat. Catal.*, 2021, **4**, 539–556.
- 9 C. Jehanno, J. W. Alty, M. Roosen, S. De Meester, A. P. Dove, E. Y.-X. Chen, F. A. Leibfarth and H. Sardon, *Nature*, 2022, **603**, 803–814.
- 10 R. Meys, A. Kätelhön, M. Bachmann, B. Winter, C. Zibunas, S. Suh and A. Bardow, *Science*, 2021, **374**, 71–76.
- 11 F. Vidal, E. R. van der Marel, R. W. F. Kerr, C. McElroy, N. Schroeder, C. Mitchell, G. Rosetto, T. T. D. Chen, R. M. Bailey, C. Hepburn, C. Redgwell and C. K. Williams, *Nature*, 2024, **626**, 45–57.
- 12 A. Dhaini, V. Hardouin-Duparc, A. Alaaeddine, J.-F. Carpentier and S. M. Guillaume, *Prog. Polym. Sci.*, 2024, **149**, 101781.
- 13 R. A. Gross and B. Kalra, *Science*, 2002, **297**, 803–807.
- 14 M. Hong and E. Y. X. Chen, *Trends Chem.*, 2019, **1**, 148–151.



15 K. W. Meereboer, M. Misra and A. K. Mohanty, *Green Chem.*, 2020, **22**, 5519–5558.

16 H.-M. Müller and D. Seebach, *Angew. Chem., Int. Ed. Engl.*, 1993, **32**, 477–502.

17 B. Laycock, P. Halley, S. Pratt, A. Werker and P. Lant, *Prog. Polym. Sci.*, 2013, **38**, 536–583.

18 A. Sangroniz, J.-B. Zhu, X. Tang, A. Etxeberria, E. Y.-X. Chen and H. Sardon, *Nat. Commun.*, 2019, **10**, 3559.

19 D. K. Bedade, C. B. Edson and R. A. Gross, *Molecules*, 2021, **26**, 3463.

20 H. Park, H. He, X. Yan, X. Liu, N. S. Scrutton and G.-Q. Chen, *Biotechnol. Adv.*, 2024, **71**, 108320.

21 A. H. Westlie, E. C. Quinn, C. R. Parker and E. Y.-X. Chen, *Prog. Polym. Sci.*, 2022, **134**, 101608.

22 G. J. M. de Koning and P. J. Lemstra, *Polymer*, 1993, **34**, 4089–4094.

23 J. Bruckmoser, S. Pongratz, L. Stieglitz and B. Rieger, *J. Am. Chem. Soc.*, 2023, **145**, 11494–11498.

24 H.-Y. Huang, W. Xiong, Y.-T. Huang, K. Li, Z. Cai and J.-B. Zhu, *Nat. Catal.*, 2023, **6**, 720–728.

25 M. S. Young, A. M. LaPointe, S. N. MacMillan and G. W. Coates, *J. Am. Chem. Soc.*, 2024, **146**, 18032–18040.

26 X. Tang and E. Y.-X. Chen, *Nat. Commun.*, 2018, **9**, 2345.

27 E. C. Quinn, A. H. Westlie, A. Sangroniz, M. R. Caputo, S. Xu, Z. Zhang, M. Urgun-Demirtas, A. J. Müller and E. Y.-X. Chen, *J. Am. Chem. Soc.*, 2023, **145**, 5795–5802.

28 X. Tang, A. H. Westlie, L. Caporaso, L. Cavallo, L. Falivene and E. Y.-X. Chen, *Angew. Chem., Int. Ed.*, 2020, **59**, 7881–7890.

29 X. Tang, A. H. Westlie, E. M. Watson and E. Y.-X. Chen, *Science*, 2019, **366**, 754–758.

30 Z. Zhang, E. C. Quinn, J. L. Olmedo-Martínez, M. R. Caputo, K. A. Franklin, A. J. Müller and E. Y.-X. Chen, *Angew. Chem., Int. Ed.*, 2023, **62**, e202311264.

31 G. B. McKenna, G. Hadzioannou, P. Lutz, G. Hild, C. Strazielle, C. Straupe, P. Rempp and A. J. Kovacs, *Macromolecules*, 1987, **20**, 498–512.

32 J. Roovers, *Macromolecules*, 1985, **18**, 1359–1361.

33 J. Roovers, *Macromolecules*, 1988, **21**, 1517–1521.

34 P. G. Santangelo, C. M. Roland, T. Chang, D. Cho and J. Roovers, *Macromolecules*, 2001, **34**, 9002–9005.

35 M. Kapnistos, M. Lang, D. Vlassopoulos, W. Pyckhout-Hintzen, D. Richter, D. Cho, T. Chang and M. Rubinstein, *Nat. Mater.*, 2008, **7**, 997–1002.

36 R. Pasquino, T. C. Vasilakopoulos, Y. C. Jeong, H. Lee, S. Rogers, G. Sakellariou, J. Allgaier, A. Takano, A. R. Brás, T. Chang, S. Goofsen, W. Pyckhout-Hintzen, A. Wischnewski, N. Hadjichristidis, D. Richter, M. Rubinstein and D. Vlassopoulos, *ACS Macro Lett.*, 2013, **2**, 874–878.

37 Y. Doi, K. Matsubara, Y. Ohta, T. Nakano, D. Kawaguchi, Y. Takahashi, A. Takano and Y. Matsushita, *Macromolecules*, 2015, **48**, 3140–3147.

38 D. Richter, S. Goofsen and A. Wischnewski, *Soft Matter*, 2015, **11**, 8535–8549.

39 J. Roovers, in *Cyclic Polymers*, ed. J. A. Semlyen, Springer Netherlands, Dordrecht, 2002, pp. 347–384, DOI: [10.1007/0-306-47117-5_10](https://doi.org/10.1007/0-306-47117-5_10).

40 M. Hong and E. Y.-X. Chen, *Nat. Chem.*, 2016, **8**, 42–49.

41 J. A. Kaitz, C. E. Diesendruck and J. S. Moore, *J. Am. Chem. Soc.*, 2013, **135**, 12755–12761.

42 H. Li, J. Ollivier, S. M. Guillaume and J.-F. Carpentier, *Angew. Chem., Int. Ed.*, 2022, **61**, e202202386.

43 J.-B. Zhu, E. M. Watson, J. Tang and E. Y.-X. Chen, *Science*, 2018, **360**, 398–403.

44 F. M. Haque and S. M. Grayson, *Nat. Chem.*, 2020, **12**, 433–444.

45 W. Jeong, J. L. Hedrick and R. M. Waymouth, *J. Am. Chem. Soc.*, 2007, **129**, 8414–8415.

46 M. L. McGraw, R. W. Clarke and E. Y.-X. Chen, *J. Am. Chem. Soc.*, 2021, **143**, 3318–3322.

47 L. Zhou, L. T. Reilly, C. Shi, E. C. Quinn and E. Y.-X. Chen, *Nat. Chem.*, 2024, **16**, 1357–1365.

48 N. Nasongkla, B. Chen, N. Macaraeg, M. E. Fox, J. M. J. Fréchet and F. C. Szoka, *J. Am. Chem. Soc.*, 2009, **131**, 3842–3843.

49 B. Zhang, H. Zhang, Y. Li, J. N. Hoskins and S. M. Grayson, *ACS Macro Lett.*, 2013, **2**, 845–848.

50 M. Ball, Y. Zhong, B. Fowler, B. Zhang, P. Li, G. Etkin, D. W. Paley, J. Decatur, A. K. Dalsania, H. Li, S. Xiao, F. Ng, M. L. Steigerwald and C. Nuckolls, *J. Am. Chem. Soc.*, 2016, **138**, 12861–12867.

51 Z. Miao, A. M. Esper, S. S. Nadif, S. A. Gonsales, B. S. Sumerlin and A. S. Veige, *React. Funct. Polym.*, 2021, **169**, 105088.

52 J. E. Poelma, K. Ono, D. Miyajima, T. Aida, K. Satoh and C. J. Hawker, *ACS Nano*, 2012, **6**, 10845–10854.

53 M. Romio, L. Trachsel, G. Morgese, S. N. Ramakrishna, N. D. Spencer and E. M. Benetti, *ACS Macro Lett.*, 2020, **9**, 1024–1033.

54 C. Hu, E. Louisy, G. Fontaine and F. Bonnet, *J. Polym. Sci., Part A: Polym. Chem.*, 2017, **55**, 3175–3179.

55 H. Jacobson, C. Beckmann and W. Stockmayer, *J. Chem. Phys.*, 1950, **18**, 1607–1612.

56 H. Jacobson and W. H. Stockmayer, *J. Chem. Phys.*, 1950, **18**, 1600–1606.

57 H. R. Kricheldorf, S. M. Weidner and F. Scheliga, *Polym. Chem.*, 2020, **11**, 2595–2604.

58 J. Ochs, C. A. Pagnacco and F. Barroso-Bujans, *Prog. Polym. Sci.*, 2022, **134**, 101606.

59 J. A. Semlyen, *Cyclic polymers*, Springer, 2000.

60 Y. Tezuka, *Topological Polymer Chemistry: Progress of Cyclic Polymers in Syntheses, Properties and Functions*, 2012.

61 H. R. Kricheldorf and S.-R. Lee, *Macromolecules*, 1995, **28**, 6718–6725.

62 M. Shaik, J. Peterson and G. Du, *Macromolecules*, 2019, **52**, 157–166.

63 S. Impemba, F. Della Monica, A. Grassi, C. Capacchione and S. Milione, *ChemSusChem*, 2020, **13**, 141–145.



64 Q. Liu, C. Meermann, H. W. Görlitzer, O. Runte, E. Herdtweck, P. Sirsch, K. W. Törnroos and R. Anwander, *Dalton Trans.*, 2008, 6170–6178.

65 A. V. Prasad, L. P. Stubbs, Z. Ma and Z. Yinghuai, *J. Appl. Polym. Sci.*, 2012, **123**, 1568–1575.

66 A. Duda and A. Kowalski, in *Handbook of Ring-Opening Polymerization*, 2009, pp. 1–51.

67 R. Anwander, in *Lanthanides: Chemistry and Use in Organic Synthesis*, ed. S. Kobayashi, Springer Berlin Heidelberg, Berlin, Heidelberg, 1999, pp. 1–61.

68 J.-B. Zhu and E. Y.-X. Chen, *Angew. Chem., Int. Ed.*, 2018, **57**, 12558–12562.

69 M. Rubinstein, *Phys. Rev. Lett.*, 1986, **57**, 3023–3026.

